Dynamic Modeling of Encrust Formation and Mitigation Strategy in a Continuous Plug Flow Crystallizer

Aniruddha Majumder[†] and Zoltan K. Nagy[*,‡,†]

Department of Chemical Engineering, Loughborough University, Loughborough LE11 3TU, UK, and School of Chemical Engineering Purdue University, West Lafayette, IN 47907-2100, USA

E-mail: zknagy@purdue.edu

Phone: +1 765 494 0734. Fax: +1 765 494 0805

Abstract

Encrustation, also known as fouling or scale formation, on the wall of plug flow crystallizers (PFC) can cause major operational and economic problems in pharmaceutical industries. These include increased energy requirements due to increment of thermal resistance and pressure drop, and clogging of the crystals due to reduction of flow area. In this work, a mathematical model for predicting the dynamic behavior of a PFC undergoing encrustation is presented. This model describes the formation of encrust layer by considering various mechanisms such as rate of solute transport from bulk to the wall, integration and removal due to shear stress induced by fluid turbulence. A population balance model for describing the crystallization process in the

[*]To whom correspondence should be addressed
[†]Department of Chemical Engineering, Loughborough University, Loughborough LE11 3TU, UK
[‡]School of Chemical Engineering Purdue University, West Lafayette, IN 47907-2100, USA

PFC is also coupled with the encrustation model in order to obtain the appropriate concentration profile in the PFC as well as product crystal size distribution (CSD). Based on this model, a mitigation strategy is proposed that relies on injection of pure solvent to dissolve the encrust layer.

Keywords: fouling, crystallization, dynamic model, encrustation, encrustation mitigation, plug flow crystallizer, population balance model

Introduction

The formation of unwanted crystal layers on the inner surface of crystallizer, stirrer or in situ sensors is known as encrustation, scale formation or crystallizer fouling. Fouling in general is one of the most important problems encountered in heat exchanger equipments that can occur due to deposition of suspended solids, insoluble salts, biological substances etc.[1–3] Encrustation is also a very common problem encountered in various type of crystallization such as cooling, evaporation, antisolvent and precipitation crystallizations.[4] This article focus only on the dynamic modeling and simulation aspects of fouling that occurs in plug flow crystallizer (PFC).

In a pharmaceutical or chemical industry, producing crystals of specific size and shape distribution, polymorphic forms and purity is very critical as they directly influence the efficiency of the subsequent downstream processes (e.g., filtration, drying, tableting) and quality of the final product (e.g., bioavailability, effectiveness, shelflife). Thus it is very important that operating conditions during crystallization can be controlled to produce crystals of required specifications.[5] Among other factors that can be sources of disturbances during crystallization such as impurity and change in feed conditions, encrustation can also be a major problem in maintaining product specifications. The encrust layer on the crystallizer surfaces developed over time increases the thermal resistance and pressure drop, making the process energy inefficient, reduces the residence time of the slurry or even causes unplanned

shutdown of the process due to clogging. Thus, understanding the encrust formation during crystallization and mitigation strategies are crucial from the viewpoint of process operation, economics and product quality maintenance.

The driving force required for the encrustation to occur is supersaturation which can be generated by cooling, heating, antisolvent addition or chemical reaction depending on the modes of crystallization. It is found that at high supersaturation, the solid surface may initiate encrustation by catalyzing primary nucleation. Conversely, at a reasonably low supersaturation collision of the crystals with the solid surface may initiate encrustation.[6] Crystal nucleation, deposition and growth may also occur simultaneously.

Encrust formation in the crystallization process would usually involve several processes[1]

1. Induction or delay period, which is the time required for the deposition process to start after the crystallizer is started

2. Transport of the solute molecules from the bulk fluid to the heat transfer surface through diffusion

3. Attachment and deposition of the solute molecules on the heat transfer surfaces which may act as sites for nucleation

4. Removal of the encrust due to shear stress imposed by fluid flow, erosion, detachment etc

5. Change in the properties of the deposited layer with time due to aging

In this work, the aging process is ignored which is more important in other type of fouling such as in crude oil deposition. The first general model to describe the fouling process was proposed by Kern and Seaton[7]. In that model, it is assumed that the time evolution of the encrust mass can be expressed by an exponential profile. This is owing to the interplay between the two competing mechanisms *i.e.*, accumulation of encrust from crystallization and removal of the encrust due to hydrodynamically induced shear stress. An enhancement

in fluid velocity would thus be accompanied by two opposing effects. It will enhance the mass transfer coefficient resulting from turbulence which promotes encrustation. Conversely, the increase shear stress on the encrust fluid interface will reduce the possibility of integration of the solute molecules. Thus, depending on the dominance of the two mechanisms, an increase in fluid velocity may increase or decrease encrust formation rate.

Recently Zhou et al.[8] investigated the layer crystallization in an annular crystallizer which is conceptually similar to scale formation. In their work, the emphasis was on avoiding some time consuming downstream processes such as washing, filtration and drying by utilizing layer crystallization followed by dissolution that produces solution of pure compound. They did not consider the modeling of evolution of crystal size distribution (CSD) during crystallization process. Moreover, laminar flow was maintained inside the crystallizer and the removal term due to the shear stress imposed by fluid flow was ignored.

The crystallization fouling model used in this paper are based on the work by Bohnet[9] and Brahim et al.[10]. This model takes into account the two competing mechanisms discussed earlier by incorporating supersaturation, mass transfer coefficient, crystallization rate constant, fluid shear stress and shear strength of the crystals. Novelty of this work is two fold: first, a dynamic encrustation model is used to investigate the encrust formation in a PFC. Secondly, population balance model (PBM) describing crystallization process is coupled with the encrustation model through mass balance. PBM is a model framework widely used for modeling the evolution of size distribution of particulate systems including crystallization process.[11] To the best of our knowledge, this is the first time a coupled PBM and encrust formation model is used for describing the crystallization process in a PFC.

Dynamic simulation of continuous crystallization is performed, which can be very useful in process design, optimal operation and control purposes. The simulation studies presented in this paper can be used not only to describe the rate of encrust formation, but also to predict how the product crystal properties (*e.g.*, mean size) are affected due to encrustation. Moreover, simulation studies on a mitigation strategy, which is based on dissolution

of the encrust layer using pure solvent, is presented. This allows us to decide when to stop crystallization in a given PFC segment and carry out cleaning or dissolution of the crust formed. The solvent flowrate and time needed to clean the PFC can also be obtained from dynamic simulations. Based on the time required for each crystallization and cleaning cycle, plant wide optimal operation can be scheduled. The dynamic model presented is useful in controlling the product crystal properties by countering disturbances such as changes in feed condition, while also taking into account fouling in the crystallizer. Additionally, the model enables the design of dynamic operating procedures that can lead to maximization of the crystallization cycles between necessary steps of cleaning due to fouling.

Model development

In this work a single PFC segment of length Z is considered. The assumptions used in this study are follows

1. A plug flow model is used to describe the fluid flow in the PFC
2. No concentration and temperature gradients in the radial direction inside the PFC
3. Axial and radial temperature gradients present at the PFC wall and encrust
4. Heat transfer takes place across the PFC wall whose outer surface is maintained at a constant temperature
5. Change of the physical properties of the solution, encrust and tube are negligible in the operating temperature range
6. Constant volumetric flow rate along the PFC

The first two assumptions are for ideal plug flow reactor. These two assumptions can be met closely in the laboratory and in industrial practice. High Reynolds number flow in sufficiently long tubes, i.e. tubes of high length/diameter ratio, will usually approximate

well the plug flow reactor. Flow in packed beds can also be treated as plug flow. The main modes of heat transfer at the PFC wall and the encrust domain is conduction. Thus, due to the symmetric nature of the heat of conduction, the temperature gradient with respect to the angular coordinate can be neglected. The temperature of the outer surface of the PFC wall can be maintained at a constant temperature by employing a water jacket with sufficient water flow. If the operating temperature range is not large, the change in physical properties of the solution, encrust and tube wall can be neglected. However, one needs to be careful about the condition at which the physical parameters of these domains are estimated, and the temperature range where they can be used. Finally, the constant volumetric flow rate through the PFC can be maintained by a constant volume pump.

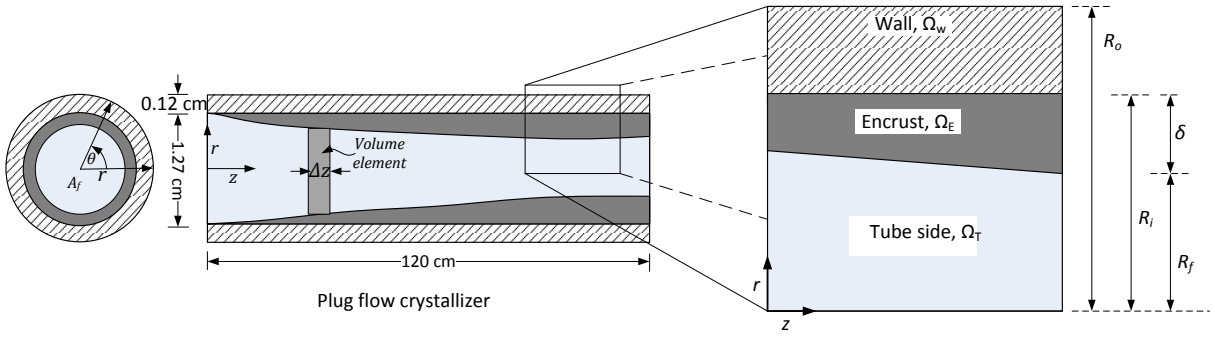

Figure 1: Cross section of the PFC showing different domains, adapted from Coletti and Macchietto[3]. Here R_o is the outer wall radius, R_i inner wall radius, $R_{\mathrm{f}}(z)$ is the flow radius and $\delta(z)$ is the thickness of the encrust.

The cross section of the PFC is shown in Figure 1 where the three domains PFC wall (Ω_{W}), encrust (Ω_{E}) and tube side (Ω_{T}) are indicated. The model used here for encrust formation is based on the fouling model by Bohnet[9] and Brahim et al.[10]. In this model, the net amount of solute deposition on the crystallizer surfaces is calculated by considering various contributing processes: transport of the solute molecules from the bulk fluid to heat transfer surface, attachment and deposition of the solute molecules on the surface to form encrust layer, removal of the encrust due to shear stress due to fluid flow. Modeling of these steps are discussed next.

Encrust formation

The rate of transport of the solute molecules through the boundary layer due to mass transfer can be modeled as

$$\frac{dm_{\mathrm{t}}}{dt} = k_{\mathrm{m}}(C_{\mathrm{b}} - C_{\mathrm{E}}); \tag{1}$$

where m_{t} is the mass of the solute transported to per unit area of the encrust layer, k_m is the mass transfer coefficient, C_{b} is the bulk fluid concentration and C_{E} is the concentration at the phase boundary between the encrust and viscous sublayer. The rate of deposition or integration of the solute molecules on the crystal lattice of the encrust is given as

$$\frac{dm_{\mathrm{d}}}{dt} = k_{\mathrm{R}}(C_{\mathrm{E}} - C_{\mathrm{sat}})^{l}; \tag{2}$$

where m_{d} is the mass of the solute deposited on the encrust layer, C_{sat} is the saturation concentration, k_{R} is the surface reaction rate constant and l is the order of surface reaction. The typical value of l lies between 1 and 2 in most of the industrial cases[9]. The Arrhenius approach can be used to calculate the k_{R} as follows

$$k_{\mathrm{R}} = k_{\mathrm{R0}} \exp(-\frac{E}{RT_{\mathrm{f}}}); \tag{3}$$

where k_{R0} is the reaction constant, E is the activation energy and T_{f} is the surface temperature of the encrust which can be calculated as[3]

$$T_{\mathrm{f}} = T + 0.55(T_{\mathrm{E}}\Big|_{r=R_{\mathrm{f}}(z)} - T). \tag{4}$$

For a mass transfer controlled reaction, it can be assumed that all the solute molecules that are transported to the phase boundary, take part in the surface reaction.[10] Such assumption has been found to describe the experimental observation of encrustation reasonably well that

occurs during crystallization of $CaSO_4$.[10] Then we have

$$\frac{dm_{\mathrm{t}}}{dt} = \frac{dm_{\mathrm{d}}}{dt}. \tag{5}$$

Now C_{E} can be eliminated using eqs.(1) and (2) and the expression for deposition rate becomes

$$\frac{dm_{\mathrm{d}}}{dt} = k_{\mathrm{m}} \left[\frac{1}{2}\frac{k_{\mathrm{m}}}{k_{\mathrm{R}}} + (C_{\mathrm{b}} - C_{\mathrm{sat}}) - \left(\frac{1}{4}\frac{k_{\mathrm{m}}^2}{k_{\mathrm{R}}^2} + \frac{k_{\mathrm{m}}}{k_{\mathrm{R}}}(C_{\mathrm{b}} - C_{\mathrm{sat}}) \right)^{1/2} \right]. \tag{6}$$

In the above derivation, surface reaction order is taken as $l = 2$. The removal term of the encrust can be calculated by considering the shear resistance of the layer which must be overcome by the shear stress acting on the surface of the encrust for removal. The shear resistance is given by[9]

$$\sigma_f = K_1 \frac{P}{N\delta(1 + \alpha\Delta T)d_p}, \tag{7}$$

where K_1 is a constant, P describes the intercrystalline adhesion forces, N is the number of fault points in the fouling layer, α is the linear expansion coefficient, δ is the thickness of the encrust, ΔT is the temperature difference between the wall and encrust surfaces and d_p is the particle diameter on the encrust surface. Following equation describes the rate of removal of solid material from the encrust layer[9]

$$\frac{dm_{\mathrm{r}}}{dt} = K_2 \frac{\tau_f}{\sigma_f} \rho_E \left(\frac{\eta g}{\rho_L} \right)^{1/3}, \tag{8}$$

where m_{r} is the mass of the solute removed per unit area of the encrust layer, K_2 is constant, $\tau_f \propto \rho_L w^2$ is the shear stress by liquid flow on encrust layer, η is the viscosity of the liquid phase, g is the gravitational acceleration and w is the fluid velocity responsible for mixing. This equation essentially shows that the rate of removal is proportional to the shear stress

acting on the encrust layer and inversely proportional to the shear strength of the encrust layer. By substituting the value for σ_f from eq. (7) in the above equation, we obtain the final expression for the removal rate as follows

$$\frac{dm_{\mathrm{r}}}{dt} = \frac{K}{P}\rho_{\mathrm{E}}(1+\alpha\Delta T)d_p(\rho_{\mathrm{L}}^2\eta g)^{1/3}w^2\delta, \tag{9}$$

$$\frac{P}{K} = 83.2w^{0.54}, \tag{10}$$

where K is a constant. Further details of the model describing removal rate can be found in Bohnet[9]. Now the net rate of increase of the material in the encrust can be calculated by taking the difference of the eqs. (6) and (9)

$$\frac{dm}{dt} = \frac{dm_{\mathrm{d}}}{dt} - \frac{dm_{\mathrm{r}}}{dt}, \tag{11}$$

$$\frac{dm}{dt} = k_{\mathrm{m}}\left[\frac{1}{2}\frac{k_{\mathrm{m}}}{k_{\mathrm{R}}} + (C_{\mathrm{b}} - C_{\mathrm{sat}}) - \left(\frac{1}{4}\frac{k_{\mathrm{m}}^2}{k_{\mathrm{R}}^2} + \frac{k_{\mathrm{m}}}{k_{\mathrm{R}}}(C_{\mathrm{b}} - C_{\mathrm{sat}})\right)^{1/2}\right] - \frac{K}{P}\rho_{\mathrm{E}}(1+\alpha\Delta T)d_p(\rho_{\mathrm{L}}^2\eta g)^{1/3}w^2\delta. \tag{12}$$

The thermal resistance χ is related to solid deposit per unit encrust area as follows

$$m = \rho_{\mathrm{E}}\delta = \rho_{\mathrm{E}}k_{\mathrm{E}}\chi. \tag{13}$$

Substituting the expressions for m and δ in terms of χ from eq. (13), eq.(12) can be written as

$$\frac{d\chi}{dt} = \frac{k_{\mathrm{m}}}{\rho_{\mathrm{E}}k_{\mathrm{E}}}\left[\frac{1}{2}\frac{k_{\mathrm{m}}}{k_{\mathrm{R}}} + (C_{\mathrm{b}} - C_{\mathrm{sat}}) - \left(\frac{1}{4}\frac{k_{\mathrm{m}}^2}{k_{\mathrm{R}}^2} + \frac{k_{\mathrm{m}}}{k_{\mathrm{R}}}(C_{\mathrm{b}} - C_{\mathrm{sat}})\right)^{1/2}\right] - \frac{K}{P}(1+\alpha\Delta T)d_p(\rho_{\mathrm{L}}^2\eta b)^{1/3}w^2\chi. \tag{14}$$

The governing equation for the encrust thickness δ can be expressed as

$$\frac{d\delta}{dt} = k_{\mathrm{E}} \frac{d\chi}{dt}, \tag{15}$$

Where k_{E} is the thermal conductivity of the encrust layer. The mass transfer coefficient can be calculated using a semiempirical approach from the Sherwood number[12]

$$\mathrm{Sh} = 0.034 \mathrm{Re}^{0.875} \mathrm{Sc}^{1/3}, \tag{16}$$

$$\mathrm{Sh} = \frac{2R_{\mathrm{f}}(z)k_{\mathrm{m}}}{D},\ \mathrm{Re} = \frac{2R_{\mathrm{f}}(z)w\rho_{\mathrm{L}}}{\eta},\ \mathrm{Sc} = \frac{\eta}{\rho_{\mathrm{L}}D}. \tag{17}$$

Here Sh is the Sherwood number, Re is the Reynolds number and Sc is the Schmidt number. While considering dissolution, a simpler model is used to track the change in thermal resistance as follows

$$\frac{d\chi}{dt} = k_{\mathrm{d}}(C_{\mathrm{b}} - C_{\mathrm{sat}}), \tag{18}$$

where k_{d} is the dissolution rate constant. Then, the change in encrust thickness can be calculated using Eqn. (15)

Energy balance

Tube wall

At the tube wall domain $\Omega_{\mathrm{W}} = \{(r, z) : r \in [R_{\mathrm{i}}, R_o], z \in [0, Z]\}$, standard heat conduction equation is used assuming symmetry with respect to the angular coordinate θ. Then the thermal balance equation without any source term becomes

$$\frac{\rho_{\mathrm{W}} c_{p,\mathrm{W}}}{k_{\mathrm{W}}} \frac{\partial T_{\mathrm{W}}}{\partial t} = \frac{1}{r}\frac{\partial T_{\mathrm{W}}}{\partial r} + \frac{\partial^2 T_{\mathrm{W}}}{\partial r^2} + \frac{\partial^2 T_{\mathrm{W}}}{\partial z^2}, \tag{19}$$

here ρ_{W} is the wall density, $c_{p,\mathrm{W}}$ is the wall specific heat capacity, $T_{\mathrm{W}}(z,r)$ is the wall temperature and k_{W} is the wall thermal conductivity.

Encrust

Similar to PFC wall, the encrust or deposition domain $\Omega_{\mathrm{E}} = \{(r,z) : r \in [R_{\mathrm{f}}(z), R_{\mathrm{i}}], z \in [0, Z]\}$ is also modeled as conduction domain. Symmetry with respect to θ is assumed. Thus, in the absence of source terms the thermal balance equation can be written as

$$\frac{\rho_{\mathrm{E}} c_{p,\mathrm{E}}}{k_{\mathrm{E}}} \frac{\partial T_{\mathrm{E}}}{\partial t} = \frac{1}{r}\frac{\partial T_{\mathrm{E}}}{\partial r} + \frac{\partial^2 T_{\mathrm{E}}}{\partial r^2} + \frac{\partial^2 T_{\mathrm{E}}}{\partial z^2}, \tag{20}$$

where ρ_{E} is the encrust density, $c_{p,\mathrm{E}}$ is the encrust specific heat capacity, $T_{\mathrm{E}}(z,r)$ is the encrust temperature and k_{W} is the encrust thermal conductivity.

It can be seen in Figure 1 that the flow radius $R_{\mathrm{f}}(z)$ is related to encrust thickness $\delta(z)$ as follows

$$R_{\mathrm{f}}(z) = R_{\mathrm{i}} - \delta. \tag{21}$$

As the encrust layer grows or dissolves, the boundary of the encrust domain Ω_{E} changes. In order to handle this moving boundary while solving Eq. (20), it is convenient to reformulate it in terms of dimensionless radial coordinate $\tilde{r}$. A coordinate transformation can be utilized for this purpose as follows[3]

$$\tilde{r} = \frac{r - R_{\mathrm{i}}}{R_{\mathrm{f}} - R_{\mathrm{i}}} = \frac{R_{\mathrm{i}} - r}{\delta}, \tag{22}$$

so that

$$\text{at } r = R_{\mathrm{i}},\ \tilde{r} = 0, \tag{23}$$

$$\text{at } r = R_{\mathrm{f}}(z),\ \tilde{r} = 1. \tag{24}$$

Note that in the newly defined coordinate, the base is at R_{i} and direction is reversed. In terms of the newly defined coordinate $\tilde{r}$, Eq. (20) can be written as

$$\frac{\partial T_{\mathrm{E}}}{\partial t} = \frac{k_{\mathrm{E}}}{\rho_{\mathrm{E}} c_{p,\mathrm{E}}} \left[\frac{1}{R_{\mathrm{i}} - \tilde{r}\delta} \left(\frac{-1}{\delta} \right) \frac{\partial T_{\mathrm{E}}}{\partial \tilde{r}} + \frac{1}{\delta^2} \frac{\partial^2 T_E}{\partial \tilde{r}^2} + \frac{\partial^2 T_{\mathrm{E}}}{\partial z^2} \right]. \tag{25}$$

Tube side

In the tube side domain $\Omega_{\mathrm{E}} = \{(r, z) : r \in [0, R_{\mathrm{f}}(z)], z \in [0, Z]\}$ the main modes of heat transfer are the convection and conduction along the axial direction and heat transfer through the encrust domain. The flow area of the tube changes with time as the encrust layer thickness changes. This change in flow area needs to be considered while deriving the governing equations for heat transfer. The details of the derivation are shown in the Supporting Information. The final form of the thermal balance equation can be written as

$$\begin{aligned} \frac{\partial}{\partial t}(A_{\mathrm{f}} T) = -\frac{\partial}{\partial z}(u A_{\mathrm{f}} T) + \frac{k}{\rho_L c_p} \frac{\partial}{\partial z}(A_{\mathrm{f}} \frac{\partial T}{\partial z}) + \frac{2\pi R_{\mathrm{f}}(z) h}{\rho_L c_p}(T_{\mathrm{E}}\big|_{R_{\mathrm{f}}(z)} - T) \\ + \frac{\rho_c \phi_v}{\rho_L c_p} \frac{(-\Delta H_c)}{M_{\mathrm{W}}} \frac{\partial}{\partial t}(A_{\mathrm{f}} \mu_3). \end{aligned} \tag{26}$$

here $A_{\mathrm{f}} = \pi R_{\mathrm{f}}^2$ is the flow area, h is the overall heat transfer coefficient, ΔH_c is the heat of crystallization and M_{W} is the molecular weight of the crystal.

Boundary conditions

At the interface between the tube wall Ω_{W} and encrust Ω_{E}, there is continuity of heat flux and temperature

$$-k_{\mathrm{W}} \frac{\partial T_{\mathrm{W}}}{\partial r}\bigg|_{r=Ri} = -k_{\mathrm{E}} \left(\frac{-1}{\delta} \right) \frac{\partial T_{\mathrm{E}}}{\partial \tilde{r}}\bigg|_{\tilde{r}=0}, \tag{27}$$

$$T_{\mathrm{W}}\big|_{r=Ri} = T_{\mathrm{E}}\big|_{\tilde{r}=0}. \tag{28}$$

At interface between the encrust Ω_{E} and tube side Ω_{T}, there is continuity of heat flux, and the inlet temperature of the feed is known.

$$-k_{\mathrm{E}}\left(\frac{-1}{\delta}\right)\frac{\partial T_{\mathrm{E}}}{\partial \tilde{r}}\bigg|_{\tilde{r}=1} = -h\left(T_{\mathrm{E}}\Big|_{r=R_{\mathrm{f}}(z)} - T\right) \tag{29}$$

$$T\Big|_{z=0} = T_{\mathrm{in}}. \tag{30}$$

Population balance model for crystallization

In order to calculate the encrust thickness in Eq. (15), the concentration inside the PFC is required. Thus, the governing equations for encrustation has to be coupled with the crystallization model which is represented by population balance and mass balance equations. The change in flow area in the tube side due to encrust formation has to be taken into account while deriving these balance equations (shown in the Supporting Information). The PBE for one size coordinate and one spatial coordinate can be written as

$$\frac{\partial}{\partial t}(A_{\mathrm{f}}n) + \frac{\partial}{\partial z}(uA_{\mathrm{f}}n) + \frac{\partial}{\partial L}(GA_{\mathrm{f}}n) = 0, \tag{31}$$

$$\text{B.C. : } G(S)n(L,z,t)\Big|_{L=0} = B_0(S), \tag{32}$$

$$n(L,z,t)\Big|_{z=0} = n_{\mathrm{seed}}(L), \tag{33}$$

where n is the CSD, G is crystal growth rate, u is the mean flow velocity, n_{seed} is the seed distribution at the feed, B_0 is the nucleation rate. The kinetic equations for growth and nucleation are presented in the simulation study section. The mass balance equation that takes into account the change in solution concentration due to crystallization as well as encrustation can be written as follows

$$\frac{\partial}{\partial t}(A_{\mathrm{f}}C) = -\frac{\partial}{\partial z}(uA_{\mathrm{f}}C) - \frac{\rho_c}{\rho_{\mathrm{L}}}\phi_v\frac{\partial}{\partial t}(A_{\mathrm{f}}\mu_3) - 2\pi\frac{\rho_{\mathrm{E}}}{\rho_L}(R_{\mathrm{i}}-\delta)\frac{\partial \delta}{\partial t}, \tag{34}$$

where ϕ_v is the volume shape factor for the crystals. The encrust density (ρ_{E}) can be calculated by combining crystal density (ρ_{c}), liquid phase density (ρ_{L}) and encrust void fraction (ϵ) as follows

$$\rho_{\mathrm{E}} = (1 - \epsilon)\rho_{\mathrm{c}} + \epsilon\rho_{\mathrm{L}}. \tag{35}$$

The encrust formation, energy balance and population balance models are then solved simultaneously since they are coupled through various interactions. The coupling of these model is shown in Figure 2.

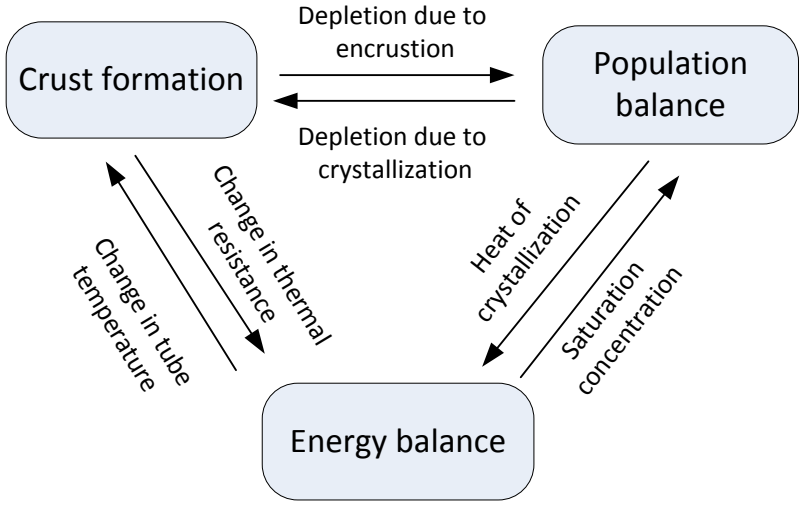

Figure 2: Coupling of the crust formation, population balance and energy balance.

Pressure can be an important parameter that may affect crystallization, in particular when the pressure is much higher than the atmospheric pressure. For example, with increasing pressure, growth rate of glucose isomerase was significantly enhanced, while the growth rate of tetragonal lysozyme crystal decreased.[13] Similarly, the nucleation rate for glucose isomerase is found to increased drastically as the pressure is increased from 0.1 to 100 MPa,[14] while the nucleation rate for subtilisin is found to decrease by a factor of 60 as the pressure is increased from 0.1 to 34 MPa.[15] In the model described above, the momentum balance was not tracked to calculate the pressure drop, since within the length of the PFC that was considered here, the pressure drop is not expected to be in the order of MPa. However, if the PFC is so long that the pressure drop is several MPa, then one needs to incorporate the

momentum balance in the model and take into account changes in crystallization kinetics due change in pressure along the PFC.

High resolution finite volume method for solving PBEs

The governing equations described in the previous section need to be solved numerically in the most practical cases. The most challenging governing equation for this purpose is the PBE describing crystallization process. This is because the PBEs are hyperbolic partial differential equations (PDEs) where sharp changes or discontinuities in the CSD can be encountered in the solution domain. In addition, the CSD can span several orders of magnitude. It is a well known fact that the first order spatial discretization schemes provide dispersive solution while the higher order spatial discretization schemes can produce numerical oscillations when a sharp change or discontinuity is encountered in the solution domain. In this work, the widely used high resolution finite volume (HRFV) method is used for solving the PBE which is designed to provide second order accuracy when the solution is smooth and avoids numerical dispersion.[16] The particular type of HRFV method implemented here is the combination of the semidiscrete FV technique with the van Leer flux limiter.[16–18] The flux limiter functions are used to approximate the flux terms at the boundary of a volume element by utilizing the cell average values from the neighboring cells. The discretization of the solution domain is shown in Figure 3.

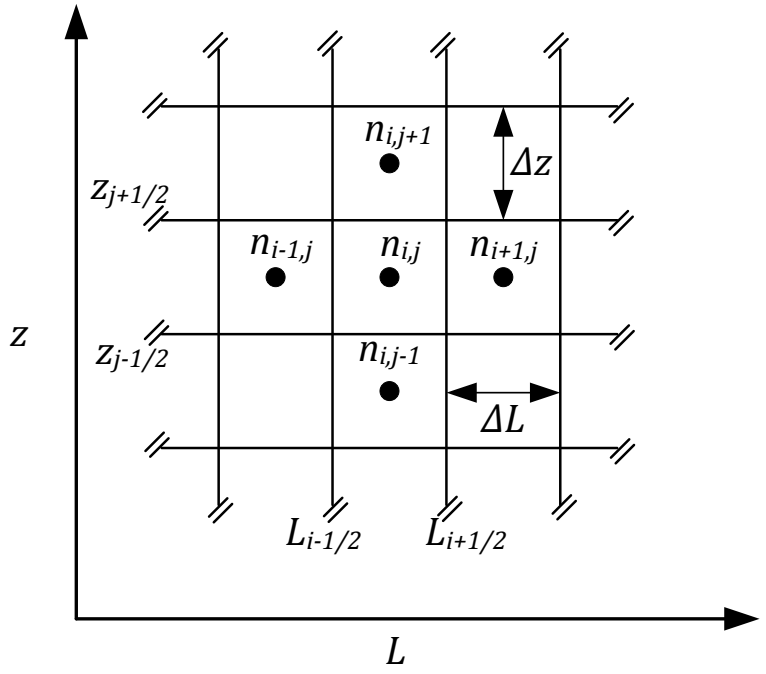

Figure 3: Finite volume discretization of the solution domain showing cell average of the CSD and the nearest neighbors.

In order to elucidate the HRFV method, let us consider the following PBE describing crystallization in a PFC

$$\frac{\partial}{\partial t}n + \frac{\partial}{\partial z}(un) + \frac{\partial}{\partial L}(Gn) = 0, \tag{36}$$

$$\text{B.C.} : G(S)n(L,z,t)\Big|_{L=0} = B_0(S), \tag{37}$$

$$n(L,z,t)\Big|_{z=0} = n_{\text{seed}}(L), \tag{38}$$

In this method, first the cell average of the CSD is defined as follows

$$n_{i,j} = \frac{1}{\Delta L \Delta z}\int_{L_{i-\frac{1}{2}}}^{L_{i+\frac{1}{2}}}\int_{z_{j-\frac{1}{2}}}^{z_{j+\frac{1}{2}}} n dL dz, \tag{39}$$

where ΔL and ΔL are the intervals used to discretise the solution domain along the crystal

size and axial distance axes, respectively. With this definition, the PBE in eq (36) reduces to a set of ODEs as follows

$$\frac{dn_{i,j}}{dt} = -\frac{1}{\Delta L}\left(Gn\big|_{i+\frac{1}{2},j} - Gn\big|_{i-\frac{1}{2},j}\right) - \frac{1}{\Delta z}\left(un\big|_{i,j+\frac{1}{2}} - un\big|_{i,j-\frac{1}{2}}\right). \tag{40}$$

The expressions for fluxes at the cell boundary, *e.g.*, $Gn\big|_{i+\frac{1}{2},j}$, require $n_{i+\frac{1}{2},j}$, $n_{i,j+\frac{1}{2}}$ which are approximated from the neighboring cell average values.

$$n_{i+\frac{1}{2},j} = n_{i,j} + \phi(r_{i+\frac{1}{2},j})(n_{i+1,j} - n_{i,j}), \tag{41}$$

$$n_{i,j+\frac{1}{2}} = n_{i,j} + \phi(r_{i,j+\frac{1}{2}})(n_{i,j+1} - n_{i,j}), \tag{42}$$

where ϕ is the flux limiter which is a function of smoothness of the CSD. The smoothness can be quantified by the ratio of the gradients of the average CSD in the two consecutive cells as follows

$$r_{i+\frac{1}{2},j} = \frac{n_{i,j} - n_{i-1,j} + e}{n_{i+1,j} - n_{i,j} + e}, \tag{43}$$

$$r_{i,j+\frac{1}{2}} = \frac{n_{i,j} - n_{i,j-1} + e}{n_{i,j+1} - n_{i,j} + e}, \tag{44}$$

where e is a small number (typically $\approx 10^{-10}$) to avoid division by zero. Then the van Leer flux limiter is written as[17]

$$\phi(r_{i+\frac{1}{2},j}) = \frac{r_{i+\frac{1}{2},j} + |r_{i+\frac{1}{2},j}|}{1 + |r_{i+\frac{1}{2},j}|}, \tag{45}$$

$$\phi(r_{i,j+\frac{1}{2}}) = \frac{r_{i,j+\frac{1}{2}} + |r_{i,j+\frac{1}{2}}|}{1 + |r_{i,j+\frac{1}{2}}|}. \tag{46}$$

It is to be noted that flux approximations given by eqs. (41)-(42) are not valid for the cells located at the boundary of the solution domain. For example, evaluation of $n_{1+\frac{1}{2},j}$ would require $n_{0,j}$ which is non existent. This problem is typically circumvented by first order

approximation for the boundary cells. Also, flux at the inlet is obtained from boundary condition. Thus, flux evaluation for the boundary cells can be summarized as follows

$$\text{if } i = 0: \; n_{i+\frac{1}{2},j} = \frac{B_{0,j}}{G_{0,j}}, \tag{47}$$

$$\text{if } i = 1: \; n_{i+\frac{1}{2},j} = \frac{n_{i,j} + n_{i+1,j}}{2}, \tag{48}$$

$$\text{if } i = N_L: \; n_{i+\frac{1}{2},j} = n_{N_L,j}, \tag{49}$$

$$\text{if } j = 0: \; n_{i,j+\frac{1}{2}} = n_{\text{seed}}, \tag{50}$$

$$\text{if } j = 1: \; n_{i,j+\frac{1}{2}} = \frac{n_{i,j} + n_{i,j+1}}{2}, \tag{51}$$

$$\text{if } j = N_z: \; n_{i,j+\frac{1}{2}} = n_{i,N_z}, \tag{52}$$

where N_L and N_z are the number of grid points used along L and z axes, respectively. Now comparing the PBEs shown in eqs. (31) and (36), it can be seen that the flow area of the PFC A_{f} appears in the PBE in eq. (31). In order to implement HRFV for this PBE, we can redefine the CSD in eq. (31) as follows

$$\hat{n} = A_{\text{f}} n, \tag{53}$$

so that it reduces the standard form of PBE given by eq. (36).

The other governing equations can be discretised using finite difference technique to obtain corresponding ODEs. Finally, the resulting set of ODEs can be solved by any accurate and efficient solver. In this work, the 'ode15s' solver available in Matlab is used which is a variable order solver based on numerical differentiation formulas.

Simulation studies

The cooling crystallization of potash alum-water system is considered in a special type of PFC known as continuous oscillatory baffled crystallizer (COBC). The COBC is a tubular

crystallizer with periodically spaced orifice baffles in order to promote mixing.[19] The COBC considered here is made of pyrex glass with dimensions of length 120 cm, internal diameter 1.27 cm and wall thickness 0.12 cm (shown in Figure 1). An oscillatory flow of the fluid is superimposed on the net flow that creates the turbulence required for mixing. While the residence time is determined by the net flow, the heat and mass transfers due to mixing are determined by the oscillatory flow. If the turbulence were solely generated by the net flow in the crystallizer, a very long tube would be required to accommodate a realistic residence time. By introducing oscillatory flow, one can thus circumvent the need for very long tubular crystallizer that would otherwise be needed while turbulence is solely generated by the net flow. Due to the oscillatory flow and the repeating cycles of vortices, strong radial motions are created that provide uniform mixing in each interbaffle zone.[19] This condition cumulatively approximates plug flow conditions closely along the length of the tube at mean flows that would otherwise result in laminar flow regimes. The flow area $A_{\mathrm{f}}(z)$ changes with time as encrustation occurs which in turn affects the amplitude of oscillation and local fluid velocity. Thus, for COBC the appropriate fluid velocity $w(z)$ responsible for mixing is calculated as

$$w(z) = 2\pi f \lambda(z), \tag{54}$$

here f is the frequency and $\lambda(z)$ is the amplitude of oscillation. The dependence of $\lambda(z)$ on flow area can be obtained from the expression of constant volumetric flow rate along the PFC as follows

$$\lambda(z) = \frac{A_{\mathrm{f},0}}{A_{\mathrm{f}}(z)}\lambda_0, \tag{55}$$

where $A_{\mathrm{f},0}, \lambda_0$ are the flow area and amplitude of oscillation, respectively at $t = 0$, *i.e.*, when no encrust is present. Since the flow area decreases with the formation of encrust layer ($A_{\mathrm{f},0} > A_{\mathrm{f}}(z)$), it follows from eq. (55) that $\lambda(z) > \lambda_0$. Thus, the local velocity $w(z)$ is larger at the location where flow area is smaller. Accordingly the appropriate Reynolds number for

COBC can be defined as[19]

$$\mathrm{Re}_o = \frac{(2\pi f \lambda(z))(2R_\mathrm{f}(z))\rho_\mathrm{L}}{\eta}, \tag{56}$$

here Re_o is the oscillatory Reynolds number calculated from oscillatory velocity responsible for mixing. The frequency and amplitude of oscillation used in this study are $f = 2\ \mathrm{s}^{-1}$ and $\lambda = 0.04$ m, respectively. The COBC is 1.2 m long and volumetric flow rate is 100 ml/min.

Simulation of encrust formation

The feed to the crystallizer is saturated solution at 40°C and contains seed with following distribution

$$n_\mathrm{seed} = \frac{\kappa}{\sigma_\mathrm{seed}\sqrt{2\pi}} \exp\left(-\frac{(L-\mu_\mathrm{seed})^2}{\sigma_\mathrm{seed}^2}\right). \tag{57}$$

where $\kappa = 1 \times 10^{10}$ is a scaling factor corresponding to 1.88% of seed mass, $\sigma_\mathrm{seed} = 15 \times 10^{-6}$ m is the standard deviation and $\mu_\mathrm{seed} = 54 \times 10^{-6}$ m is the mean size. Nucleation, growth and dissolution kinetics for potash alum-water system are taken from Shoji et al.[20]. Both the primary and secondary nucleation rates are considered as follows

$$J_\mathrm{prim} = j_\mathrm{a} \exp\left[-\frac{j_\mathrm{b}}{T^3(\ln S)^2}\right], \tag{58}$$

$$J_\mathrm{sec} = k_\mathrm{b} M_\mathrm{T}^j (C - C_\mathrm{sat})^b, \tag{59}$$

where M_T is the magma density, S is the supersaturation ration and σ is the relative supersaturation defined as

$$S = \frac{C}{C_\mathrm{sat}}, \tag{60}$$

$$\sigma = \frac{C}{C_\mathrm{sat}} - 1. \tag{61}$$

The total nucleation is the sum of the primary and secondary nucleation rates. The empirical crystal growth rate expression is written as a function of relative supersaturation, temperature and crystal size[20]

$$G = K_{\mathrm{G}} \exp\left(-\frac{\Delta E_{\mathrm{g}}}{RT}\right) \times \left[1 - \exp\left\{-\gamma(L+\beta)\right\}\right] \sigma^{g_1}, \tag{62}$$

where K_{G} is the growth rate constant, ΔE_{g} is the activation energy. The parameters for growth and nucleation kinetics are given in Table 1.

Table 1: Kinetic parameters

Parameter	Value	Units
j_{a}	1.70×10^{8}	$\#\mathrm{m}^{-3}\mathrm{s}^{-1}$
j_{b}	5.64×10^{6}	K^{3}
k_{b}	3.14×10^{7}	$\#\mathrm{m}^{-3}\mathrm{s}^{-1}$
j	1	-
b	1.32	-
K_{G0}	2.05×10^{5}	ms^{-1}
γ	7.18×10^{2}	-
β	6.10×10^{-5}	m
ΔE_{g}	5.77×10^{4}	J mol^{-1}
g_1	1.42	-

However, parameters for encrust formation for this system are not available. In order to perform the simulation studies, experimentally determined parameters for another inorganic salt $CaSO_4$ were used in this study except for higher values for reaction rate constant to emphasize encrust formation. The heat of crystallization is assumed to be negligible compared to the other contributing terms in energy balance. The parameters used for simulating encrust formation along with the reference are shown in Table 2. The simulations were performed on a PC with an Intel Core i5-3570 processor (3.40 GHz, 8 GB RAM) using Matlab. The number of grid points used was 20 along axial, radial and size axes.

Table 2: Parameters used in simulation.

Domain	Parameter	Value	Units	Reference
Wall	ρ_W	2230	$\mathrm{kg.m^{-3}}$	pyrex glass
	$c_{p,\mathrm{W}}$	753	$\mathrm{Jkg^{-1}K^{-1}}$	pyrex glass
	k_{W}	1.005	$\mathrm{W.m^{-1}.K^{-1}}$	pyrex glass
Encrust	ρ_{E}	1750	$\mathrm{kgm^{-3}}$	potash alum
	$c_{p,\mathrm{E}}$	870	$\mathrm{Jkg^{-1}K^{-1}}$	sodium chloride
	k_{d}	1.27×10^{-3}	$\mathrm{m.s^{-1}}$	-
	k_{E}	1.11	$\mathrm{Wm^{-1}K^{-1}}$	$CaSO_4$ [9]
	K_{R0}	7.07×10^{6}	$\mathrm{m^4.kg^{-1}.s^{-1}}$	-
	d_p	36	μm	Brahim et al. [10]
	D	1.57×10^{-9}	$\mathrm{m^2/s}$	Bohnet [9]
	E	37143	$\mathrm{J.mol^{-1}}$	Brahim et al. [10]
	α	1×10^{-6}	$\mathrm{K^{-1}}$	Bohnet [9]
	η	600×10^{-6}	Pa.s	Bohnet [9]
	ϵ	0.2	-	Bohnet [9]
Tube	ρ_{L}	1080	$\mathrm{kgm^{-3}}$	water
	c_p	4185.5	$\mathrm{Jkg^{-1}.K^{-1}}$	water
	k	0.58	$\mathrm{Wm^{-1}K^{-1}}$	water
	h	1000	$\mathrm{Wm^{-2}K^{-1}}$	Shell-and-tube exchanger

The outer wall temperature is fixed at 25 °C. As the feed slurry pass through the PFC, it is cooled due to the heat transfer through the PFC wall and crystallization takes place. In Figure 4, the CSD of the seed and product are shown. The product CSD in the absence of encrustation is simulated by turning off the encrust formation arbitrarily. It can be seen in Figure 4(b) that crystals not only grows in size, but also small sized crystal appear due to nucleation resulting from significant supersaturation generated along the crystallizer by the good heat transfer. The volume average size of the crystals in this case is found to be 95 μm. Conversely, when encrust formation is considered, there is a drastic reduction in the average size of the product CSD after 4 hour as shown in Figure 4(c). The volume average size of the crystal is found to be only 69.78 μm. The comparison is also shown in Figure 4(d). This result can be attributed to the several consequences of the encrust formation such as reduction of flow area that leads to reduction in residence time and decrease of supersaturation driving force due to increase in thermal resistance and consumption of the solute due to encrust formation.

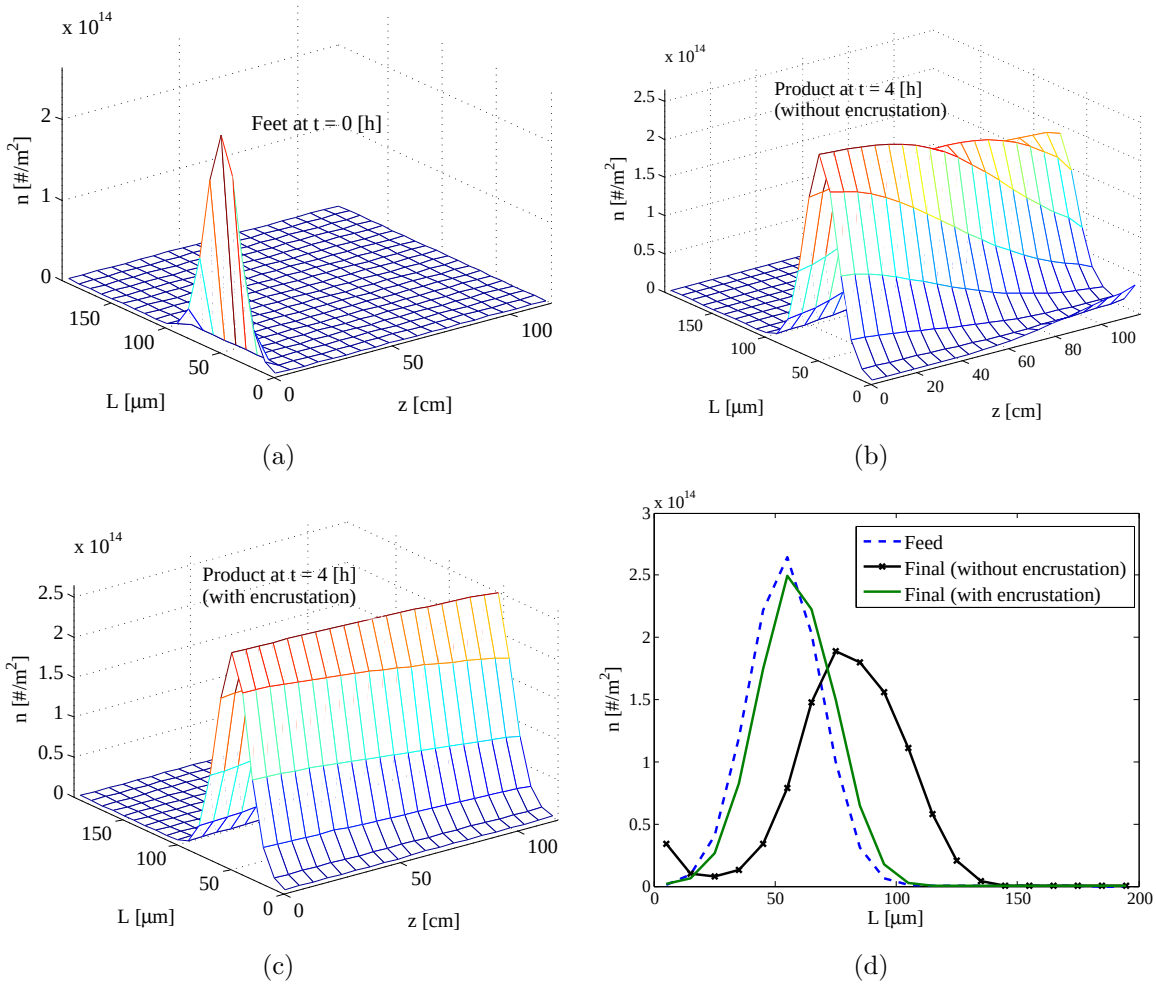

Figure 4: (a) Feed CSD at $t = 0$ h, (b) Final CSD along the crystallizer at $t = 4$ h when encrustation does not occur, (c) Final CSD along the crystallizer at $t = 4$ h when encrustation occurs (d) Comparison of the CSDs at the outlet.

The time evolution of the encrust thickness along the crystallizer and the corresponding reduction in residence time of the crystals are shown in Figure 5. It can be seen that the encrust thickness keeps on increasing with time, the maximum being near the mid way of the tube. In a 4 h operation, the encrust thickness can grow as large as 0.32 cm. Consequently, the residence time of the crystals continues to decrease from 91 s to 31 s. The sectional view of the PFC is shown in Figure 6 where development of the encrust formation is indicated for 2 h and 4 h. The maximum blockage of the flow area was found to be 59% after 2 h and 75% after 4 h as shown in Figure 6(b).

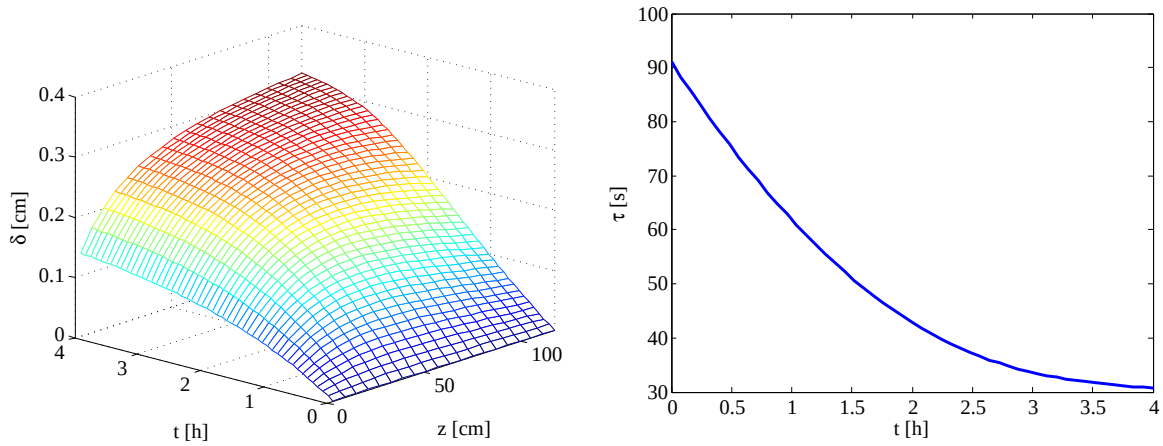

(a) (b)

Figure 5: (a) Time evolution of the encrust thickness along the crystallizer, (b) Reduction in residence time of the crystals due to encrustation.

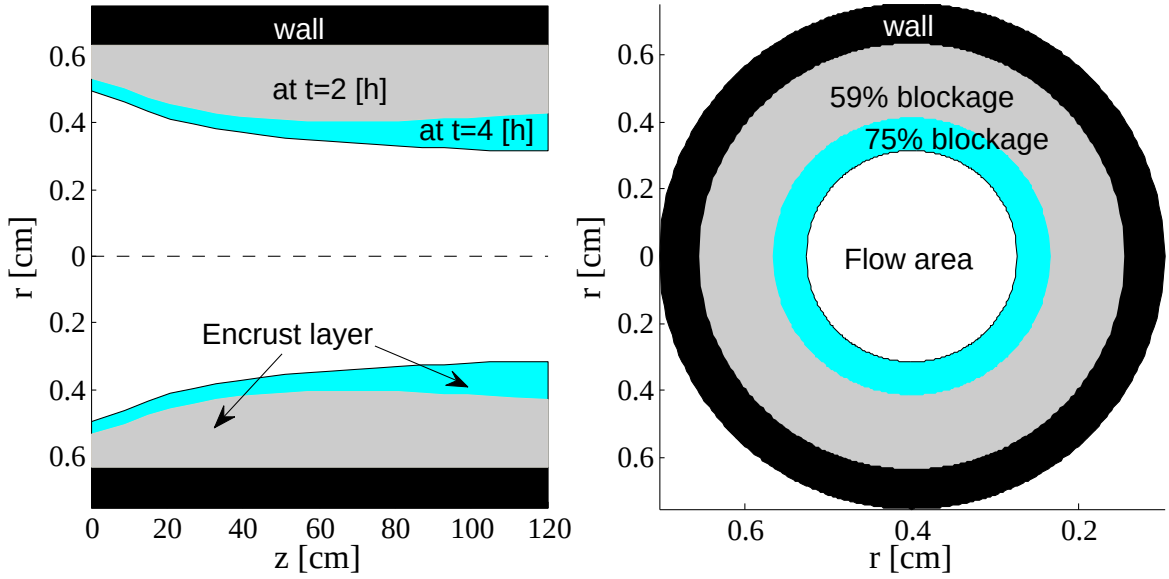

Figure 6: Reduction of the flow area due to encrust formation at $t = 2$ h and $t = 4$ h (a) Axial section (b) Cross-section.

The thermal resistance along the crystallizer due to encrust formation after 4 h is shown in Figure 7. The corresponding temperature distribution in the encrust layer is also shown. These plots suggest that a significant thermal resistance is introduced in the encrust layer and about 3.25 °C drop in the temperature is found within that layer. In Figure 8, the comparison of the tube side temperatures and corresponding supersaturation profiles are

presented for the encrust and no encrust formation cases. These temperature profiles are similar to what is seen in a tubular heat exchanger. A higher temperature drop along the crystallizer that leads to higher driving force for crystallization was found when no encrust formation takes place compared to the encrust formation case. This is in accordance of the result that a larger mean size of the crystals are found for the no encrust case. The wall temperatures for both cases are also shown in Figure 9. As expected, temperature is high near the inlet region, and significant temperature gradient is found in both axial and radial directions. The drop in temperature is larger for no encrust case.

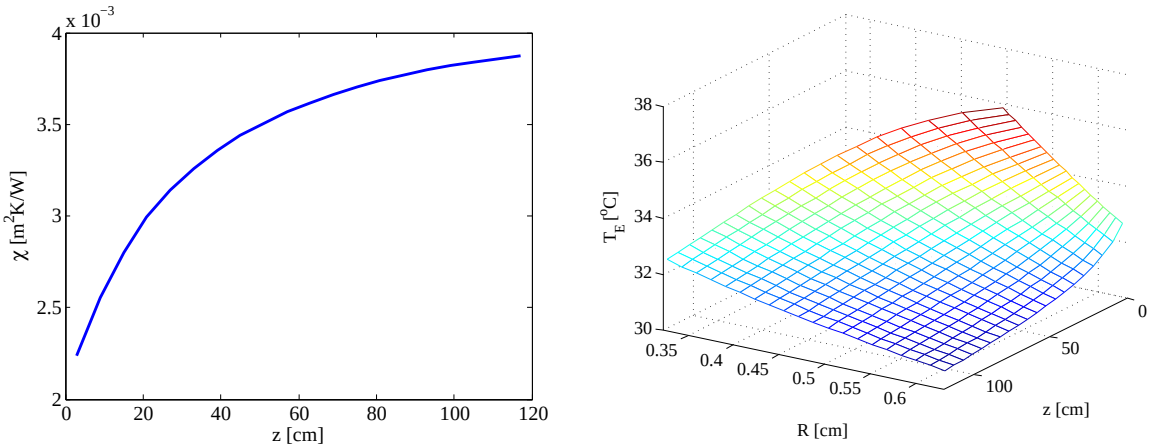

(a) (b)

Figure 7: (a) Thermal resistance of the encrust layer along the PFC at $t = 4$ h and (b) Corresponding temperature distribution in the encrust layer.

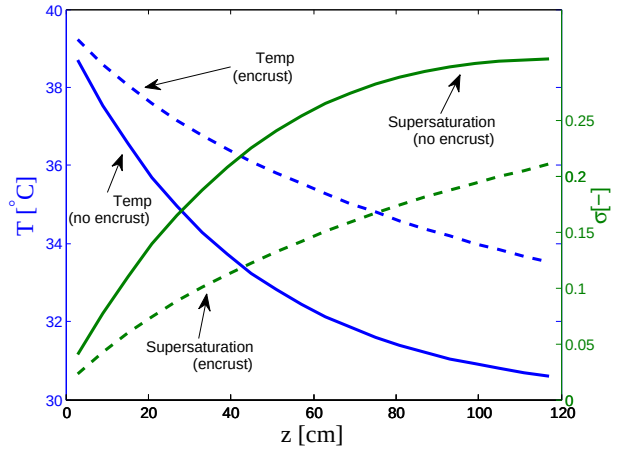

Figure 8: Comparison showing the decrease in driving force in terms of temperature gradient and supersaturation due to encrust formation. The tube side temperature (slurry temperature) without encrust decreases sharply and the corresponding supersaturation increases along the PFC due to lower heat transfer resistance between the tube side and PFC wall (solid curves). Conversely, after 4 h of operation the formed encrust layer increases the heat transfer resistance between the tube side and PFC wall. Thus, the drop in temperature along the PFC is much lower leading to lower driving force in terms of supersaturation (dashed curves).

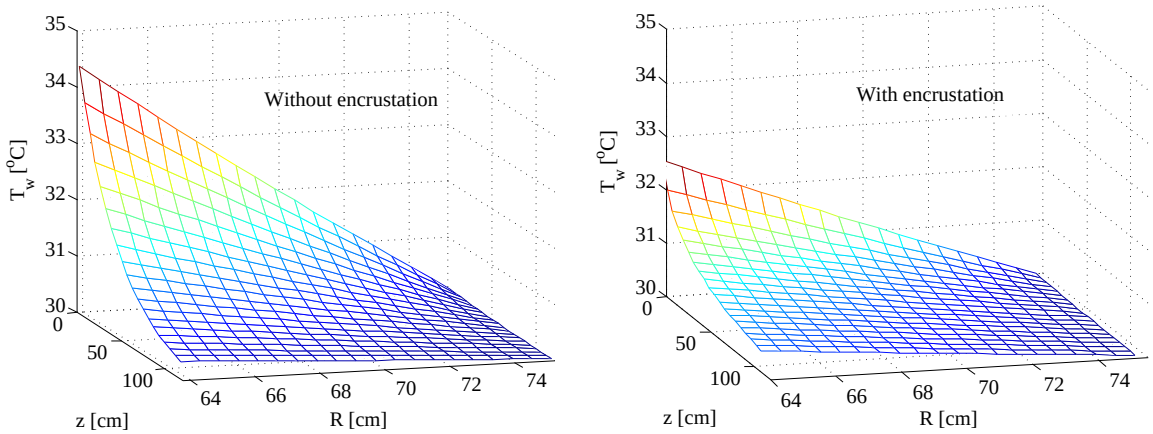

Figure 9: Comparison showing tube wall temperature profiles after 4 h of operation (a) No encrust formation, (b) Encrust formation.

The concentration profile is also shown in Figure 10. It is seen that concentration decreases at a faster rate at the early stage of crystallization for the case when encrust formation takes place as compared to the no encrust case. This initial sharp decrease in concentration

is due to the high supersaturation driving force resulting from large temperature difference. The high driving force causes rapid formation of the encrust layer, in addition to the rapid growth of the seed crystals. These two phenomena contributes to the solute consumption at a much higher rate as compared to the rate at which solute is transported by the convection of the feed stream. However, with time the increment of encrust thickness reduces the driving force which slows down the crystal growth and encrust formation. Consequently, the solute transported by convection of the feed stream largely compensates the depleted solute in the solution.

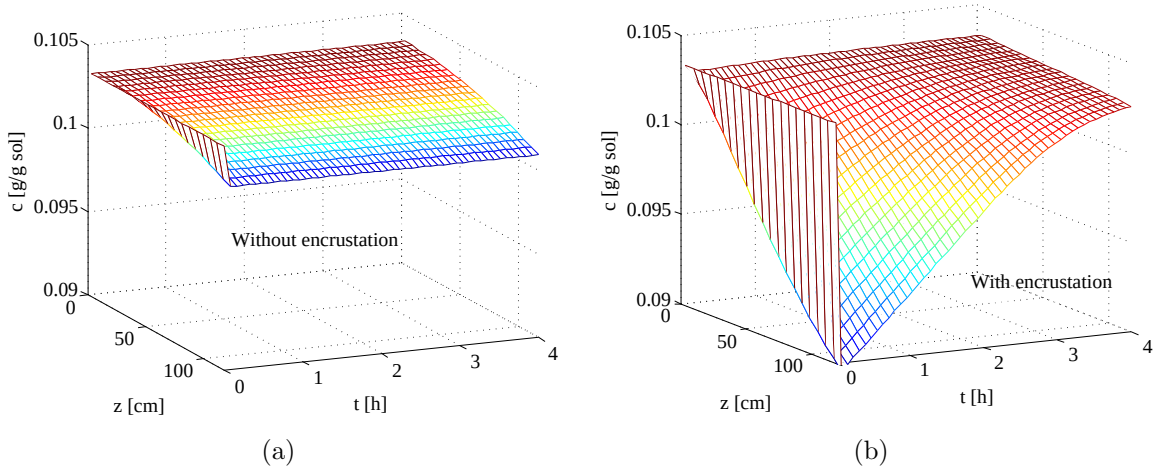

Figure 10: Comparison showing time evolution of the concentration profiles after 4 h of operation (a) No encrust formation, (b) Encrust formation

Mitigation strategy for encrustation

Various means are possible to mitigate the crystallizer fouling. These means include mechanical cleaning,[21] addition of antifoulant chemicals,[22] coating the heat transfer surface[23] and dissolving the encrust in cleaning agent.[24] The removal of the encrust layer by dissolving it using pure solvent will be discussed here, as this methodology has the provision to recycle the expensive API deposition. In the case study considered here, pure solvent at 32 °C was fed at the rate of 100 ml/min. The outer wall temperature was kept at 40 °C. In such case, the dissolution of the encrust layer takes place which is described by eq. 18. It was found

that the encrust layer was completely dissolved within 0.3 h for the parameters used. The time evolution of the encrust thickness and concentration along the crystallizer is shown in Figure 11. As can be seen in this figure, the encrust layer starts dissolving at the entrance of the crystallizer and the dissolution process moves forward with time. This happens as the solvent becomes saturated quickly due to fast dissolution of the encrust layer. This is also clear from the concentration profile in Figure 11(b), where it is seen that the concentration reaches quickly to 0.09 g/g which is the saturation concentration at the tube side temperature.

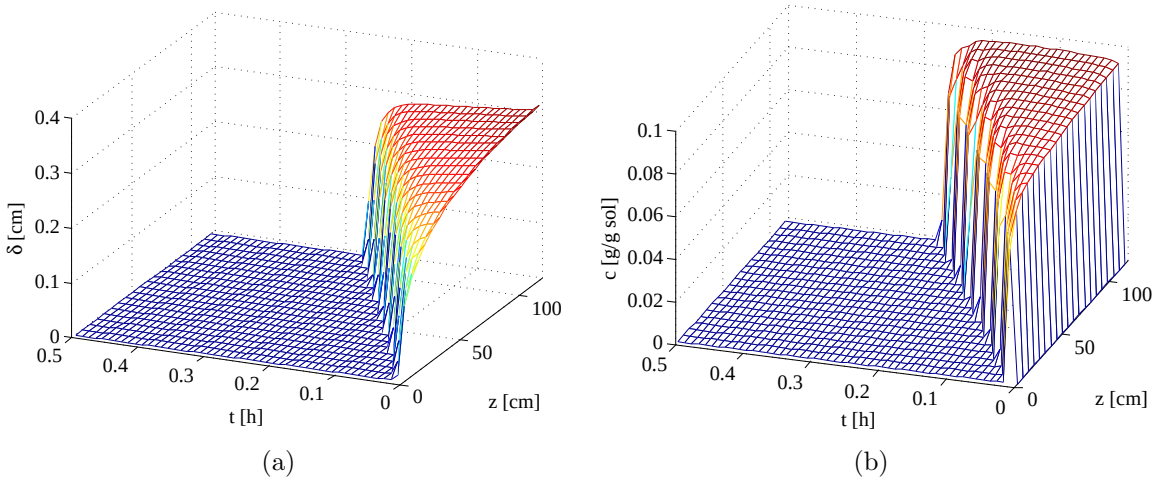

Figure 11: Figure showing dissolution profiles along the crystallizer for $t = 0.50$ h (a) Encrust thickness (b) Concentration.

Conclusions

A dynamic model of encrustation inside the plug flow crystallizer is presented which is used to predict encrust thickness, concentration and temperature profiles along the crystallizer, as well as, product crystal size distribution. This model requires coupling of encrust formation model with population balance, mass balance and energy balance equations. The population balance equation is solved using high resolution finite volume technique while the rest of the governing equations are solved using finite difference method. The simulation studies show

that the product crystal size can be affected severely when encrust formation takes place. This is due the combined effect of reduction of driving force in terms of supersaturation and reduction of the residence time of the crystals. This observation is also in line with observation found in industrial crystallization. A mitigation strategy is also proposed which involved injecting pure solvent through the crystallizer to dissolve the encrust layer. Based on these results, a more systematic studies on mitigation strategies that relies on cyclic growth and dissolution steps will be performed in future. These studies will be very useful in the industrial crystallization processes where encrustation can be a major problem in maintaining product quality and plant operating schedule.

Acknowledgement

Funding is acknowledged from the European Research Council under the European Union's Seventh Framework Programme (FP7/2007-2013)/ERC grant agreement No. [280106-CrySys].

Supporting Information Available

The derivation of the tube side energy balance, population balance and mass balance equations with variable flow area of the plug flow crystallizer.

This material is available free of charge via the Internet at `http://pubs.acs.org/`.

Notations

A_{f}	flow area, m^2
A_{n}	annular area, m^2
B_0	nucleation rate, $\#\mathrm{m}^{-2}\mathrm{s}^{-1}$
C	solute concentration, g/g of water
C_{b}	concentration at the bulk, g/g of water

C_{E}	concentration at the phase boundary between encrust and viscus sublayer, g/g of water
C_{sat}	saturation concentration, g/g of water
c_p	heat capacity of the tube side material, $\mathrm{JKg^{-1}K^{-1}}$
$c_{p,\mathrm{E}}$	heat capacity of the encrust, $\mathrm{JKg^{-1}K^{-1}}$
$c_{p,\mathrm{W}}$	heat capacity of the wall, $\mathrm{JKg^{-1}K^{-1}}$
d_{p}	particle diameter, m
D	diffusivity, $\mathrm{m^2s^{-1}}$
E	activation energy, $\mathrm{J.mol^{-1}}$
g	gravitational acceleration, $\mathrm{m^2s^{-1}}$
G	growth rate of the crystals, $\mathrm{ms^{-2}}$
h	overall heat transfer coefficient, $\mathrm{Wm^{-2}K^{-1}}$
ΔH_c	heat of crystallization, $\mathrm{J\ mol^{-1}}$
k_{d}	dissolution rate constant, $\mathrm{m^2KW^{-1}s^{-1}}$
k_{E}	heat conductivity of the encrust layer, $\mathrm{Wm^{-1}K^{-1}}$
k_{m}	mass transfer coefficient, $\mathrm{ms^{-1}}$
K_{R}	surface reaction rate constant (2nd order), $\mathrm{m^4kgs^{-1}}$
k_{E}	thermal conductivity of the encrust layer, $\mathrm{Wm^{-1}K^{-1}}$
k_{W}	thermal conductivity of the wall, $\mathrm{Wm^{-1}K^{-1}}$
L	characteristic length of crystals, m
m	net mass of the solute deposited per unit area of encrust, $\mathrm{kgm^{-2}}$
m_{d}	mass of the solute deposited per unit area of encrust, $\mathrm{kgm^{-2}}$
m_{r}	mass of the solute removed per unit area of encrust, $\mathrm{kgm^{-2}}$

m_{t}	mass of the solute transported to per unit area of the encrust layer , kgm^{-2}
M_{T}	magma density, kgm^{-3}
M_{W}	molecular weight of the crystal, g mol^{-1}
n	crystal size distribution, $\#\mathrm{m}^{-2}$
N	number of fault points within fouling layer, dimensionless
r	radial coordinate, m
R	gas constant, $\mathrm{JK}^{-1}\mathrm{mol}^{-1}$
R_{f}	flow radius, m
R_{i}	inner radius, m
R_o	outer radius, m
Re	Reynolds number, dimensionless
t	time, s
T	temperature at the tube side, °C
T_{E}	temperature at the encrust layer, °C
T_{W}	temperature at the wall, °C
u	mean fluid velocity, ms^{-1}
v	volume of a crystal, $\mu\mathrm{m}^3$
V	volume of the crystallizer, $\mu\mathrm{m}^3$
w	local fluid velocity, ms^{-1}
z	axial distance along the crystallizer, m

Greek symbols

α	linear expansion coefficient, K^{-1}
β	constant in growth rate expression, m

δ	encrust thickness, m
ϵ	voidage of the encrust layer, dimensionless
η	viscosity of the fluid, Pa.s
γ	constant in growth rate expression, m^{-1}
λ	amplitude of oscillation, m
ϕ_v	volume shape factor of the crystals, dimensionless
μ_i	i^{th} moment of distribution, m^{i-2}
Ω_{E}	encrust domain, dimensionless
Ω_{T}	tube domain, dimensionless
Ω_{W}	wall domain, dimensionless
ρ_{c}	density of the crystal, kgm^{-3}
ρ_{L}	density of the liquid, kgm^{-3}
σ	relative supersaturation, dimensionless
σ_f	shear strength of the encrust layer, Nm^{-2}
τ	residence time, s
τ_f	shear stress by liquid flow on encrust layer, Nm^{-2}
θ	angular coordinate, dimensionless
χ	encrust thermal resistance, $\mathrm{m}^2\mathrm{KW}^{-1}$

References

(1) Epstein, N. *Heat Transfer Engineering* **1981**, *4*, 43–56.

(2) Somerscales, E. F. C. *Heat Transfer Engineering* **1990**, *11*, 19–36.

(3) Coletti, F.; Macchietto, S. *Ind. Eng. Chem. Res.* **2011**, *50*, 4515–4533.

(4) Bott, T. R. *Experimental Thermal and Fluid Science* **1997**, *14*, 356–360.

(5) Nagy, Z. K.; Fevotte, G.; Kramer, H.; Simon, L. L. *Chem. Eng. Res. Des.* **2013**, *91*, 1903–1922.

(6) Vendel, M.; Rasmuson, Å. C. *AIChE Journal* **1997**, *43*, 1300–1308.

(7) Kern, D.; Seaton, R. *British Chemical Engineering* **1959**, *4*, 258–262.

(8) Zhou, L.; Su, M.; Benyahia, B.; Singh, A.; Barton, P. I.; Trout, B. L.; Myerson, A. S.; Braatz, R. D. *AIChE J.* **2013**, *59*, 1308–1321.

(9) Bohnet, M. *Chem. Eng. Technol.* **1987**, *10*, 113–125.

(10) Brahim, F.; Augustin, W.; Bohnet, M. *International Journal of Thermal Sciences* **2003**, *42*, 323–334.

(11) Ramkrishna, D. *Population balances: Theory and applications to particulate systems in engineering*; Acadamic Press, San Diego, CA, 2000.

(12) Lammers, J. Zur Kristallisation von Calciumsulfat bei der Verkrustung von Heizflächen. Ph.D. thesis, TU Berlin, 1972.

(13) Suzuki, Y.; Sazaki, G.; Miyashita, S.; Sawada, T.; Tamura, K.; Komatsu, H. *Biochimica et Biophysica Acta (BBA) - Protein Structure and Molecular Enzymology* **2002**, *1595*, 345–356.

(14) Suzuki, Y.; Maruoka, T.; Tamura, K. *High Pressure Research* **2010**, *30*, 483–489.

(15) Waghmare, R. Y.; Pan, X. J.; Glatz, C. E. *Journal of Crystal Growth* **2000**, *210*, 746–752.

(16) LeVeque, R. J. *Finite-Volume Methods for Hyperbolic Problems*; Cambridge university press, Cambridge, UK, 2002.

(17) van Leer, B. *J. Comput. Phys.* **1974**, *14*, 361–370.

(18) Majumder, A.; Nagy, Z. K. *AIChE J.* **2013**, *59*, 4582–4594.

(19) Lawton, S.; Steele, G.; Shering, P.; Zhao, L.; Laird, I.; Ni, X.-W. *Org. Process Res. Dev.* **2009**, *13*, 1357–1363.

(20) Shoji, M.; Eto, T.; Takiyama, H. *J. Chem. Eng. Jpn.* **2011**, *44*, 191–196.

(21) Stegelman, A.; Renfftlen, R. *Hydrocarbon Process.;(United States)* **1983**, *62*.

(22) Darling, D.; Rakshpal, R. *Mater. Performance* **1998**, *37*, 42–45.

(23) Müller-Steinhagen, H.; Zhao, Q. *Chem. Eng. Sci.* **1997**, *52*, 3321–3332.

(24) Jamialahmadi, M.; Mller-Steinhagen, H. *Chem. Eng. Res. Des.* **2007**, *85*, 245–255.

For Table of Contents Use Only

Dynamic Modeling of Encrust Formation and Mitigation Strategy in a Continuous Plug Flow Crystallizer

Aniruddha Majumder and Zoltan K. Nagy

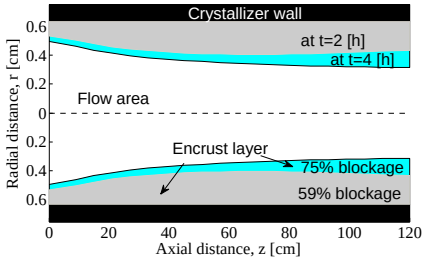

Synopsis

A dynamic framework by coupling encrust formation, population balance and energy balance models is presented which enables the prediction of encrust thickness and its effect on the product crystal size distribution in a continuous plug flow crystallizer. The dissolution of the encrust layer by injecting pure solvent is also discussed as a mitigation strategy.